





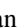




## Variance induced decoupling of spin, lattice, and charge ordering in perovskite nickelates

Alessandro R. Mazza <sup>1,2</sup> Shree Ram Acharya <sup>1</sup> Patryk Wařsik <sup>3</sup> Jason Lapano,<sup>1</sup> Jiemin Li,<sup>3</sup> Brianna L. Musico,<sup>4</sup> Veerle Keppens <sup>4</sup> Christopher T. Nelson,<sup>1</sup> Andrew F. May <sup>1</sup> Matthew Brahlek,<sup>1</sup> Claudio Mazzoli <sup>3</sup> Jonathan Pellicciari <sup>3</sup> Valentina Bisogni <sup>3</sup> Valentino R. Cooper,<sup>1</sup> and T. Zac Ward <sup>1,\*</sup>

<sup>1</sup>Materials Science and Technology Division, Oak Ridge National Laboratory, Oak Ridge, Tennessee 37831, USA

<sup>2</sup>Center for Integrated Nanotechnologies, Los Alamos National Laboratory, Los Alamos, New Mexico 87545, USA

<sup>3</sup>National Synchrotron Light Source II, Brookhaven National Laboratory, Upton, New York 11973, USA

<sup>4</sup>Department of Materials Science and Engineering, University of Tennessee, Knoxville, Tennessee 37996-4545, USA



(Received 31 January 2022; revised 23 August 2022; accepted 2 November 2022; published 6 January 2023)

Perovskite nickelates possess an intimate connection among the structural, electronic, and magnetic orders. We investigate how crystal-field disorder induced by cation size variance impacts the emergence of macroscopic magnetic, structural, and electronic behaviors in single crystal high-entropy oxide nickelate films. The degree of variation in cation sizes hosted on the lattice is found to strongly influence critical ordering temperatures. Resonant x-ray scattering and density functional theory describe how high-variance systems produce local lattice distortions that can be used to manipulate charge disproportionation. The disorder induced shifts to local structure are shown to function as a critical order parameter capable of decoupling the nickelates' distinctive magnetic ground state and metal-insulator transition from its charge ordered state, making it possible to stabilize room-temperature ordered phases not observed in low-variance ternary compounds.

DOI: [10.1103/PhysRevResearch.5.013008](https://doi.org/10.1103/PhysRevResearch.5.013008)

### I. INTRODUCTION

The perovskite nickelates ( $\text{ANiO}_3$ ) host a rich phase diagram with novel magnetic ordering and sharp first order metal-insulator transitions (MITs) closely coupled to crystal structure [1,2]. Modifications to the Goldschmidt tolerance factor through A-site sublattice populations have a dramatic influence on phase type and transition onset temperatures. This sensitivity to crystal-field effects makes these systems highly responsive to slight changes in composition and strain [3–5]; however, there is little fundamental understanding of how local frustration and distortion inhomogeneity influence the macroscopic electronic and magnetic structures [6]. Recently, this question has gained significant importance in the topotactically reduced perovskite nickelates, where local distortion effects driven by variation in the size of ionic radii on the A-site sublattice can dictate electronic phase and shape of the superconducting dome in infinite layer nickelates [7–10]. This sensitivity to cation compositional disorder is also broadly important to many correlated systems, where spin, charge, and lattice energies are near degenerate [11,12].

Theoretical models demonstrate that the electronic and magnetic structure of perovskite nickelates are often dictated by cation size by shifting local distortions, phonon coupling, and  $\text{NiO}_6$  breathing modes [13]. Variations and inhomogeneity of the cation sizes populating the A-site sublattice can

therefore provide an extra layer of tunability to phase response by breaking local symmetries and driving frustration and local charge redistributions not possible in more uniformly distorted lattices [14]. This suggests that an ability to manipulate the type and degree of variance on the A-site sublattice is likely to lead to new local interactions and unexpected responses not existing in previously explored phase diagrams [15]. However, generating large size variances through substitutional codoping can be limited by thermodynamic processes which result in like elements clustering or forming secondary phases due to enthalpic effects during synthesis [16,17]. Paradoxically, it has been shown that this limitation can be conquered by greatly increasing the diversity of cations hosted on a lattice, which allows entropy to overcome enthalpic effects and create well-mixed systems [18–20]. This has led to the stabilization of crystals hosting five or more elements on cation sites in spinels [21–23], perovskites [24–28], rocksalts [29–31], pyrochlore [32], and Ruddlesden-Popper [33–35] lattices, where the high configurational complexity often results in unexpected functionalities such as exceptional ion conductivity [36] and magnetic ordering [31,37–39].

In this work, single crystal films of the high-entropy oxide perovskite nickelate  $(\text{Y}_{0.2}\text{La}_{0.2}\text{Nd}_{0.2}\text{Sm}_{0.2}\text{Gd}_{0.2})\text{NiO}_3$  are synthesized and studied to understand the role of cation size variance in the emergence of macroscopic functionality. Y is significantly smaller than the other four lanthanide cations equiatomicly populating the A-site sublattice, which greatly increases the cation size variance. For simplicity, this high-variance perovskite nickelate is abbreviated as  $\text{HVNiO}_3$ . X-ray diffraction (XRD) and electron microscopy show that these high-variance films are single crystal and free of clustering or secondary phases. Density functional theory (DFT) is used to map the role of size variance on the functionally important octahedral rotation bond angle and predicts that

\*wardtz@ornl.gov

Published by the American Physical Society under the terms of the [Creative Commons Attribution 4.0 International](https://creativecommons.org/licenses/by/4.0/) license. Further distribution of this work must maintain attribution to the author(s) and the published article's title, journal citation, and DOI.

local configurational disorder can have a significant role in the formation of macroscopic electronic and magnetic phases. Resonant elastic x-ray scattering (REXS) provides evidence of long-range antiferromagnetic (AFM) order, while transport measurements demonstrate that the metal-insulator transition (MIT) is strongly influenced by cation size variance and leads to a higher transition temperature than the average tolerance factor would predict. Analysis of temperature dependent resistivity additionally points to the formation of a unique phase in the conducting nickel plane. Resonant inelastic x-ray scattering (RIXS) identifies inequivalent Ni-O bond lengths that distinguish this emergent phase as Ni bond disproportionation that effectively acts to decouple the electronic, lattice, spin, and charge order transitions. The reported behaviors do not conform to traditional nickelate tolerance factor phase diagrams, which demonstrates that cation size variance provides an alternative means of manipulating correlated behaviors outside of known phase spaces.

Single crystal  $\text{HVNiO}_3$  films are grown on  $(\text{LaAlO}_3)_{0.3}(\text{Sr}_2\text{TaAlO}_6)_{0.7}$  (LSAT) (001) oriented substrates using pulsed laser deposition (PLD). X-ray diffraction and reciprocal space mapping of a 40 nm film demonstrates an epitaxial single crystal under tensile strain (see Fig. 5 of the Methods section). These measurements place the lattice parameters as  $a = b = 3.82 \text{ \AA}$  and  $c = 3.773 \text{ \AA}$ , with a  $\varepsilon_{xx} = +1.2\%$ . Tensile strain is expected to impact the density of oxygen vacancies in nickelate films, affecting their resistivity, but not significantly impacting their critical temperatures relative to the bulk. Therefore, our tensile strained films are used as a reference to the bulk metal-insulator transition and Néel temperatures in  $\text{HVNiO}_3$  [3]. In Fig. 1(a), temperature dependent resistivity of  $\text{HVNiO}_3$  is used to determine the bulk metal-insulator transition temperature ( $T_{\text{MIT}}$ ). The MIT is well above room temperature with  $T_{\text{MIT}} \sim 410 \text{ K}$ . This is significantly higher than would be expected if this transition was unaffected by cation size variance, comparing to the averaged value. Apart from  $\text{LaNiO}_3$ , which is metallic at all temperatures, each of the ternary parent nickelate compounds that make up the  $\text{HVNiO}_3$  compound have MITs ranging from 585 K in  $\text{YNiO}_3$  to 200 K in  $\text{NdNiO}_3$ . From a simple consideration of the average lattice parameter of these parent nickelates, the expected MIT of  $\text{HVNiO}_3$  should be  $\sim 350 \text{ K}$ , which is 60 K lower than that observed. This increase in  $T_{\text{MIT}}$  is unexpected as cation size variance in non-nickelate  $\text{ABO}_3$  and  $\text{A}_2\text{BO}_4$  crystals is generally linked to a decrease in transition temperatures [11,40–42]. However, recent theoretical work has suggested that manipulating variance in nickelates may provide unique accessibility to structure-driven functional transitions that lie outside of traditional phase spaces [13]. Here, the Ni-O-Ni bond angles are dictated by the tolerance factor and directly related to the MIT, where an increase in  $T_{\text{MIT}}$  points to an increase in the effective bandwidth of oxygen octahedral rotations as seen in heterostructured nickelate systems [43,44].

The presence of hysteresis in the  $\text{HVNiO}_3$ 's transport data also provides important clues as to the type of phase transition occurring at 410 K. For example, the parent ternaries  $\text{NdNiO}_3$  and  $\text{PrNiO}_3$  have similar hysteresis while  $\text{SmNiO}_3$  and  $\text{YNiO}_3$  do not [3,44,45]. The suppression of the hysteresis

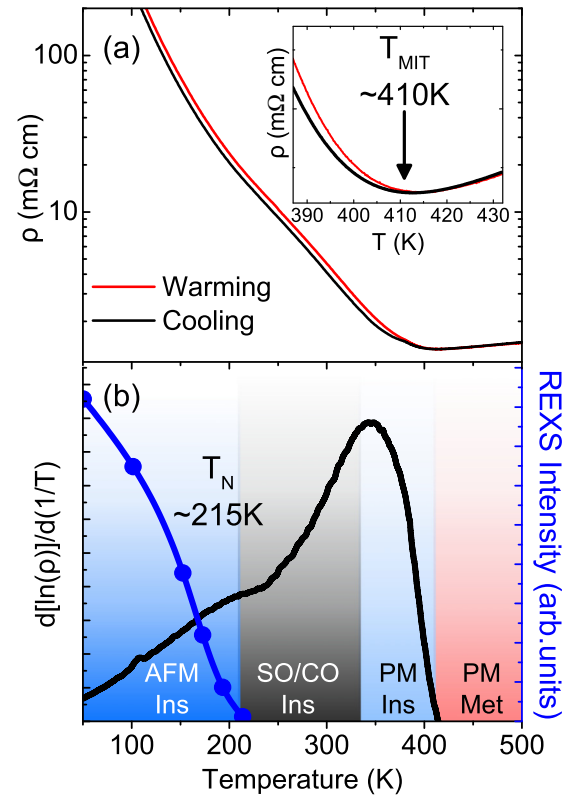


FIG. 1. Resistive and magnetic behavior of  $\text{HVNiO}_3$ . (a) Temperature dependent transport shows a clear metal-insulator transition at  $\sim 410 \text{ K}$ . (b)  $d(\ln \rho)/d(1/T)$  and resonant elastic x-ray scattering reveal the onset of magnetic order below  $T_N \sim 215 \text{ K}$ , which matches the maximum  $E'$  order parameter seen in other nickelates. An anomalous spin or charge ordered phase transition is also identified by the peak in  $d(\ln \rho)/d(1/T)$ , which appears as an intermediate phase transition prior to  $E'$  type AFM order.

is often attributed to thermal fluctuations but has also been directly correlated to whether the observed transition is first or second order. Having observed clear hysteresis, the transport data suggest a first order transition (where  $T_{\text{MIT}} = T_N$ ). With the possible exception of  $\text{LaNiO}_3$  which until recently was believed to be paramagnetic at all temperatures, ternary nickelates generally possess a low-temperature AFM state, where  $T_N \leq T_{\text{MIT}}$  [46]. The AFM order hosted in  $\text{ANiO}_3$  is unconventional with a propagation vector of  $q = (\frac{1}{4} \frac{1}{4} \frac{1}{4})$  due to inequivalent adjacent Ni sites. The change from the paramagnetic insulating phase to the spin ordered insulating phase allows  $T_N$  to be approximated by analysis of resistivity data. The peak deflection point observed in  $d(\ln \rho)/d(1/T)$  reflects the spin ordering in the insulating phase of nickelates and has been established as a tool in measuring the percolation threshold temperature of AFM in nickelates [24,47–50]. From this analysis, shown in Fig. 1(b), it appears that  $\text{HVNiO}_3$  exhibits a massive enhancement of  $T_N$  relative to other nickelates with a transition  $\sim 330 \text{ K}$ . To clarify if this transition is due to the  $E'$  AFM order observed for all other nickelates, REXS is used to observe the onset of intensity at the  $(\frac{1}{4} \frac{1}{4} \frac{1}{4})$  propagation vector in Fig. 1(b) (see Methods for details). The order parameter determines  $T_N \sim 215 \text{ K}$ , matching well with the expected value given the nickelate phase

diagram. This result suggests, supported by recent findings of magnetic ordering in  $\text{LaNiO}_3$  [46], that magnetic ordering in nickelates is not significantly influenced by the Ni-O-Ni bond angle or, as will be discussed below, variance in this bond angle. The discrepancy between the onset of this order parameter temperature and the deflection point in transport at 330 K is very unusual; and proves that in this system transport alone cannot be used to definitively confirm the magnetic order type as is widely accepted in previous nickelate studies [24,47–50]. Notably, there is a minor inflection point in transport at  $\sim 225$  K that aligns well with REXS results; however, the dominant feature at  $\sim 330$  K is a clear signature of another transition outside of the magnetic ordering.

In exploring this emergent phase transition, it is important to contextualize the known role of tolerance factors in determining structural distortions exhibited in the ternary nickelates. The native  $\text{ANiO}_3$  ( $A = \text{Y, Gd, Sm, Nd, and La}$ ) ternary parents have a range of temperature dependent electronic and magnetic phases closely tied to structure. In bulk perovskites, distortions around the transition metal centered octahedra can be predicted using the Goldschmidt tolerance factor,  $\tau = \frac{R_A + R_O}{\sqrt{2(R_B + R_O)}}$ , where  $R_A$  is the ionic radius of the A-site cation,  $R_O$  is the ionic radius of the oxygen anion, and  $R_B$  is the ionic radius of the B-site cation. Gross structural distortion types can then be predicted with  $0.7 \leq \tau \leq 0.9$  producing orthorhombic or monoclinic distortions and  $0.9 \leq \tau \leq 1$  leading to orthorhombic or rhombohedral distortions in nickelates.  $\text{YNiO}_3$  is a highly distorted monoclinic insulator at room temperature. Its tolerance factor of  $\tau = 0.863$  is the smallest of the cations at the A-site [1,24,47]. At the other extreme,  $\text{LaNiO}_3$  has the largest tolerance factor of  $\tau = 0.94$ , is rhombohedral, and is always metallic [24,46,51]. Using the  $3^+$  crystalline radii, the composition of  $\text{HVNiO}_3$  has an average cation radius of 122 pm, which gives an average tolerance factor ( $\bar{\tau}$ ) of 0.898 and a variance ( $\sigma^2$ ) of  $23.3 \text{ pm}^2$  [52,53].

Figure 2 provides a summary of the nickelate phase diagram as a function of the tolerance factor. With a calculated  $\bar{\tau} = 0.898$ , the  $T_{\text{MIT}}$  is considerably higher than would be expected if variance played no role in driving transition temperatures. Furthermore, the anomalous ordering which occurs at  $\sim 330$  K is completely unique to  $\text{HVNiO}_3$ . As a comparison, a low-variance high-entropy nickelate ( $\text{La}_{0.2}\text{Pr}_{0.2}\text{Nd}_{0.2}\text{Sm}_{0.2}\text{Eu}_{0.2}$ ) $\text{NiO}_3$  hosting only lanthanides on the A-site sublattice has a variance of  $11.2 \text{ pm}^2$  and an average tolerance factor very similar to  $\text{NdNiO}_3$ . This low-variance system was found to behave identically to the ternary material in relation to  $T_{\text{MIT}}$  and  $T_N$  and showed no evidence of anomalous ordering between these temperatures [26]. The lanthanides' relative radii uniformity appears to be below some critical threshold of size variance to trigger the increase in  $T_{\text{MIT}}$  and formation of the intermediate phase.

To understand how size variance influences local structure and Ni-O-Ni bonding distortions, DFT is used to compare  $\text{HVNiO}_3$  to a simple ternary  $\text{SmNiO}_3$  crystal, which has a similar tolerance factor but no variation in A-site size. The simulation results are shown in Fig. 3(a) for  $4 \times 10$  unit cell models. In constructing the model of  $\text{HVNiO}_3$ , the five A-site cations are randomly distributed. After the systems

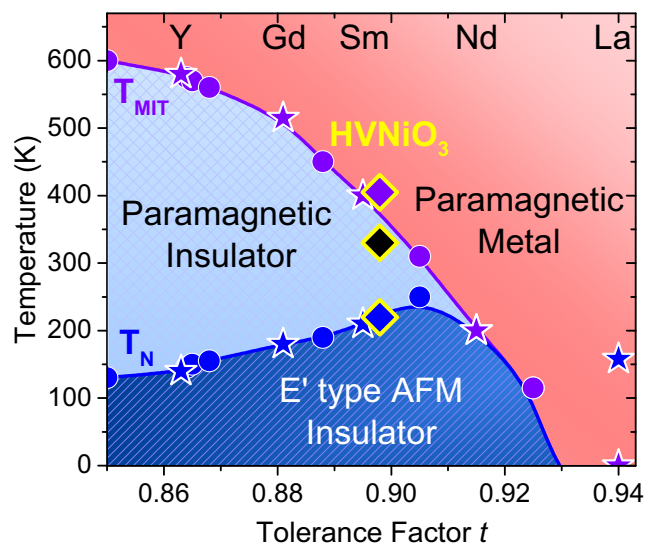


FIG. 2. The nickelate phase diagram as a function of tolerance factor including  $\text{HVNiO}_3$ . The parent ternary Y, Gd, Sm, Nd, and La nickelates are shown with star symbols while the circles are other known nickelates with the values taken from the literature [53,54].  $T_{\text{MIT}}$  (purple) and  $T_N$  (blue) for  $\text{HVNiO}_3$  are shown with diamond symbols with  $T_{\text{MIT}}$  being enhanced and the anomalous ordering being labeled by the black diamond. Compositional studies on  $\text{HVNiO}_3$  films were resolution limited to  $\sim 10\%$  uncertainty which places uncertainty of  $t$  at roughly the size of the diamond symbols.

are allowed to relax to their respective lowest-energy state, the oxygen octahedra bond angles oriented along the  $c$  axis are extracted. Figure 3(b) compares the distribution of bond angles for the two systems. In the  $\text{SmNiO}_3$ , these angles are all identical. In the  $\text{HVNiO}_3$  system, the Ni-O-Ni bond angles can vary widely and are presented in the figure as the average value of the four angles corresponding to Ni in a layer with standard deviations denoted by the error bars. The oxygen octahedral rotations are shown to be nonuniform, as a direct result of A-site cation size variance. We contrast these results with the only other high-entropy nickelate system ( $\text{La}_{0.2}\text{Pr}_{0.2}\text{Nd}_{0.2}\text{Sm}_{0.2}\text{Eu}_{0.2}$ ) $\text{NiO}_3$ , which was shown to behave as expected if considering the average size of the A-site [24]. In this system, the variance of the A-site size is a small fraction of the that hosted in  $\text{HVNiO}_3$ . We stress in comparing these two systems that the high cation size variance of the A-site is the critical ingredient in creating a distribution in Ni-O-Ni bond angles, which drive the divergence from the known nickelate phase diagram seen in  $\text{HVNiO}_3$ .

These deviations in octahedral uniformity are a likely contributor to the previously unreported phase transition from the paramagnetic insulating phase to the anomalous phase at 330 K in  $\text{HVNiO}_3$ . These distortions necessarily influence the breathing modes of the  $\text{NiO}_6$ , which dictate the exchange constants in nickelates, in turn having a significant effect on magnetic transition temperatures. Additionally, local variations in octahedral rotations can enable the charge transfer required for inequivalent Ni-O sites arising from bond disproportionation. In previous works, the combination of these effects has been induced in nickelate heterostructures, where octahedral rotations are modified by dimensionality and strain

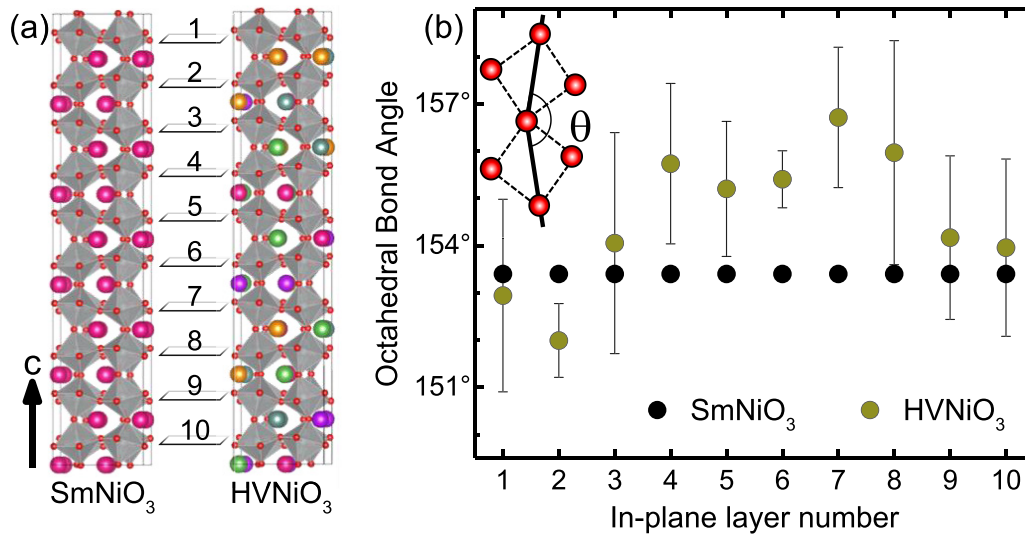


FIG. 3. (a) Atomic model of the SmNiO<sub>3</sub> and HVNiO<sub>3</sub> systems used in this study. Teal, purple, pink, yellow, green, and red spheres represent Y, Gd, Sm, Nd, La, and O atoms, respectively. Ni atoms are inside the octahedra. (b) O-Ni-O-Ni-O octahedra bond angles as a function of the unit cell number along the *c* axis. The average of the four angles in each plane in (a) is taken and their standard deviation is given by the error bars. The black line is for the SmNiO<sub>3</sub> system. The inset describes the definition of angle  $\theta$  used to quantify the octahedra rotation where the empty circles represent the O atoms on an *ab* plane.

at the interface of NdNiO<sub>3</sub>/SrTiO<sub>3</sub> [43]; however, the MIT, charge ordering, and disproportionation have always been reported as occurring in concert when present [44]. In the HVNiO<sub>3</sub> system, the observed anomalous phase occurring below the  $T_{\text{MIT}}$  at 330 K and above  $T_N$  at 215 K may be the result of decoupling of these functional phenomena.

RIXS is used to identify possible changes to the local Ni charge states that would signal the onset of charge disproportionation. Figure 4 shows the HVNiO<sub>3</sub> RIXS spectra at the Ni *L*<sub>3</sub> edge measured at different temperatures, 40, 300, and 340 K, to track the evolution of the electronic structure across the three insulating phases seen from REXS and transport

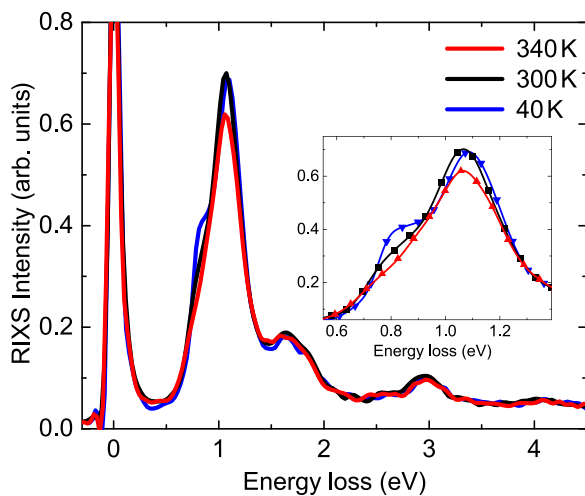


FIG. 4. Resonant inelastic x-ray scattering on HVNiO<sub>3</sub> grown on LSAT shows the Ni sites to be 3*d*<sup>8</sup>. (Inset) Emergence of the feature at  $\sim 0.8$  eV demonstrates inequivalence at the Ni sites from the *dd* excitations which signal an early onset of bond disproportionation starting near 300 K.

measurements. An energy of 853 eV is selected for the RIXS spectra as this is the location of the primary peak in the Ni *L*<sub>3</sub> absorption spectra (see Methods for details). As discussed in previous studies [2,45], the intraorbital *dd* excitations present in the RIXS spectra between 1 and 3 eV arise from the redistribution of the 3*d* electrons across the crystal-field split levels and include multiplet effects. The resulting line shape in Fig. 4 is consistent with that of a Ni 3*d*<sup>8</sup> configuration, which is typical of NiO and NdNiO<sub>3</sub> [45,54]. Important to identifying the onset of charge rebalancing, however, is the line shape variation versus temperature of the first *dd* excitation around 1 eV. Here, a lower-energy feature around 0.75 eV emerges just below  $T_{\text{MIT}}$  at 300 K and continues to strengthen as temperature is reduced below  $T_N$ . This feature was previously observed in NdNiO<sub>3</sub> and attributed to the presence of two inequivalent, bond-disproportionated Ni sites—one with elongated Ni-O bonds and another with compressed Ni-O bonds, which form a charge ordering coupled to a spin ordered transition and MIT [2]. The emergence of the 0.75 eV feature in the RIXS spectra of HVNiO<sub>3</sub> at 300 K is thus a direct consequence of the incipient formation of the bond disproportionation associated with charge order alone, as it happens well above the spin ordering transition  $T_N = 215$  K. This fingerprint of charge disproportionation in nickelates is always concurrent with the MIT, where the charge disproportionation and bond disproportionation drive the transition to an insulating state. Particularly, SmNiO<sub>3</sub> is known to have a MIT concurrent with charge/bond disproportionation which has been observed directly with x-ray absorption spectroscopy [55]. The results in the HVNiO<sub>3</sub> system demonstrate a decoupling of the MIT from charge ordering in the presence of strong *A*-site size variance, which is significantly different from all previous studies in perovskite nickelates where site-to-site cation size variance is lower.

In summary, cation size variance can be a powerful tool to directly impact oxygen octahedral rotations in nickelates,

which allows the exploitation of the close tie between structural, magnetic, and electronic phases to influence functional responses. In ternary nickelates, the metal-insulator transition has been tied to a structure transition, disproportionation, and charge ordering. In  $\text{NdNiO}_3$ , these transitions also coincide with spin ordering. This work shows that large size variance can be used to remove the necessity of a lattice shift, disproportionation, or charge ordering transition on inducing the metal-insulator transition and spin order. This is unexpected and opens untapped opportunities to understand and control these and related systems. Density functional theory shows how cation size variance can be used to drive a randomization of Ni-O-Ni bond angle distribution through the lattice. Nonequilibrium growth dynamics combined with entropy stabilization processes allows the stabilization of single crystal ( $\text{Y}_{0.2}\text{La}_{0.2}\text{Nd}_{0.2}\text{Sm}_{0.2}\text{Gd}_{0.2}$ ) $\text{NiO}_3$  films, which host a high degree of structural frustration on the *A*-site sublattice. This high variance in cation size is found to have a strong influence on the metal-insulator transition and magnetic ordering temperatures, while providing access to a room-temperature ordered phase not observed in low-variance ternary compounds. Resonant inelastic x-ray scattering reveals this transition to be the result of decoupling of the MIT and charge ordered phases where bond disproportionation leading to inequivalences in the Ni sites occurs  $>100$  K above the spin order temperature and 80 K below  $T_{\text{MIT}}$ . This work demonstrates the potential to selectively tune fundamental degrees of freedom that allow control of the charge ordering temperatures without perturbation to the normally intertwined orderings in nickelates. With this finding, the nickelate phase space may be expanded to unexplored regions by using the degree of *A*-site sublattice variance as an order parameter in the manipulation of local charge, electronic phase, and spin symmetry breaking.

## II. METHODS

### A. Synthesis

A 248 nm wavelength KrF excimer laser operating at a fluence of  $1.8\text{ J/cm}^2$  with a  $3\text{ mm} \times 5\text{ mm}$  spot size and a repetition rate of 2 Hz was used with a substrate to target a distance of 5 cm for pulsed laser deposition. Oxygen pressure and substrate temperature were held at 90 mT and  $625^\circ\text{C}$ , respectively, during growth. After growth, oxygen pressure was increased to 400 Torr before cooling to room temperature. Samples were single phase and oriented to the substrate as shown in Fig. 5. While synthesis of this composition has been attempted in bulk ceramic forms, stabilizing it as a single phase has been problematic. Thus, the ceramic target used in the PLD growth is stoichiometric to the desired film composition but hosts several crystal phases [26,56–58]. Ceramic targets were prepared using a solid-state reactor with an annealing temperature of  $1250^\circ\text{C}$  for 10 h with a ramp rate of  $5^\circ\text{C/min}$ . XRD measurements are performed on a four-circle high-resolution x-ray diffractometer (Panalytical X'Pert Pro) utilizing  $\text{Cu } K\alpha_1$  radiation. Targets were found to be stoichiometric and multiphase but produced single phase films. This is not unexpected as the entropy-stabilized phase of this compound likely requires faster quenching and/or high formation temperatures relative to those accessible in standard

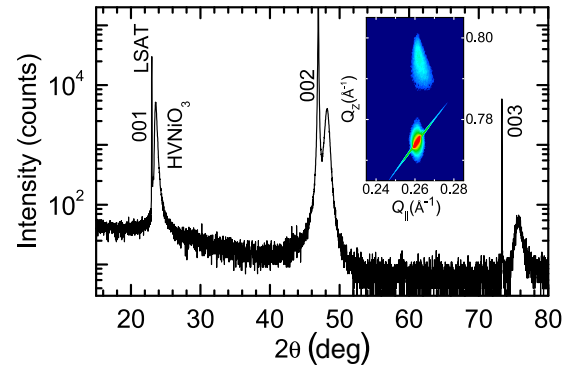


FIG. 5. XRD measurements of  $\text{HVNiO}_3$  on LSAT show film is single phase and oriented to substrate with (inset) RSM near (103) peak.

bulk synthesis approaches [39,59]. PLD is a nonequilibrium growth method. The laser pulse heats a region of the target to a near plasma state in a few nanoseconds. This plume is ejected toward the substrate and is fully quenched to the substrate temperature within a few milliseconds of its ejection from the target [60–62].

In addition to characterization of the structure at 300 K, we investigated the temperature dependence of the microstructure of the film. As in other nickelates, the MIT is expected to be coincident with an orthorhombic to monoclinic phase transition. This initiates the breathing mode distortion and comes with a contraction of the unit cell volume. In Fig. 6 we show the temperature dependent XRD of the film (002) taken in 5 K increments from 300 to 425 K. As shown, there is no change in the lattice parameter, suggesting no clear transition from orthorhombic to monoclinic microstructure in  $\text{HVNiO}_3$ .

### B. Transport

Low temperature transport measurements were carried out in a Quantum Design physical property measurement system

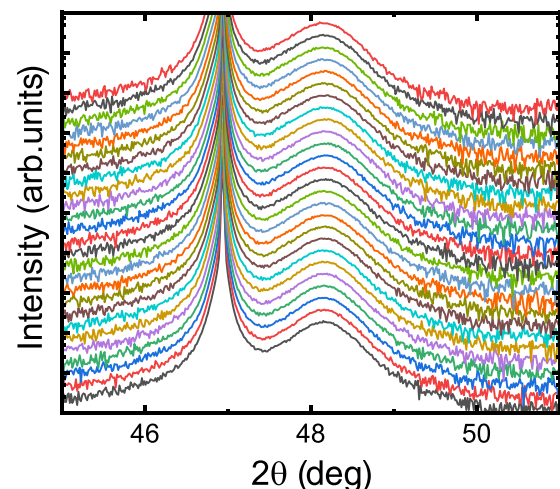


FIG. 6. Temperature dependent XRD measurements of  $\text{HVNiO}_3$  on LSAT. As shown, there is no change in the film (002) indicating no change in the film's unit cell volume as is expected in an orthorhombic to monoclinic phase transition.

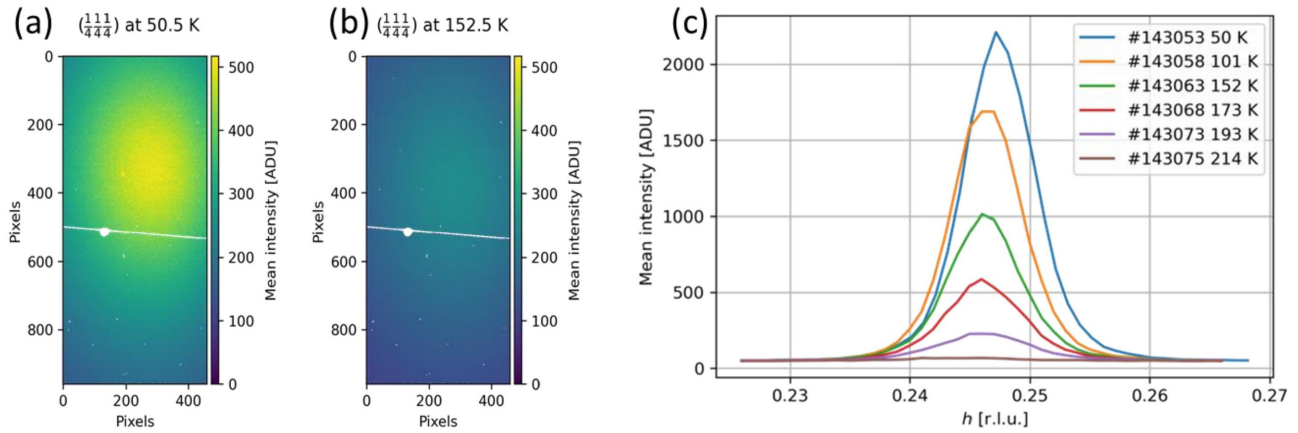


FIG. 7. Sample detector images at the  $\text{HVNiO}_3$   $(1/4\ 1/4\ 1/4)$   $E$ -type antiferromagnetic Bragg peak at 50.5 K (a) and 152.5 K (b). The integrated intensity plotted as a function of the film  $h$  direction for multiple temperatures to the disappearance of the magnetic peak  $\sim 215$  K is given in (c).

(PPMS) operating with a temperature range from 2 to 380 K. High-temperature data were measured in a tube furnace in a flowing atmosphere. Measurements in both cases were made using a four-point probe setup at a sweep rate of  $\sim 5$  K/min.  $T_N$  was determined from the anomaly in the derivative analysis  $F(T) = d(\ln \rho)/d(1/T)$  on the cooling curves of both  $\text{HVNiO}_3$  thin films, as has been previously reported [48,50]. The given tensile strain increases the resistivity of nickelates but does not impact  $T_{\text{MIT}}$  [3,48,49]; these results should reflect the bulklike  $\text{HVNiO}_3$  transition temperature.

### C. Resonant elastic x-ray scattering

The resonant elastic x-ray scattering studies were carried out at the Coherent Soft X-ray (CSX) 23-ID-1 beamline at the National Synchrotron Light Source II facility (Brookhaven National Laboratory). A fast charge-coupled device (fCCD) camera (Sydor Instruments), with  $960 \times 960$  pixels and a pixel size of  $30 \times 30 \mu\text{m}^2$ , was located 34 cm away from the sample. The sample was mounted on a wedge so that the  $[1,1,1]$  reciprocal lattice direction lay in the vertical scattering plane. The  $\pi$ -polarized x-ray beam was tuned to the  $\text{Ni } L_3$  absorption edge ( $\sim 847$  eV) to enhance the signal. The measured  $E'$  type AFM order diffraction peak was located at  $(1/4\ 1/4\ 1/4)$  in reciprocal lattice units (r.l.u.) as shown in Fig. 7. The sample was temperature cycled on a helium-flow cryostat from 50 K to well above  $T_N$  (at the cryostat). Measurements along the  $hkl$  directions were taken at about 20 min intervals to allow for the sample thermal stabilization, preceded by  $\theta/2\theta$  scans and energy scans at fixed  $\mathbf{q}$  to maximize the signal on the detector. The fCCD detector exposure was set to 2 s per image and one image per point. The magnetic peak intensity versus temperature, shown in Fig. 1(b) in arbitrary units, was calculated by first integrating the peak intensity on detector images taken at every  $hkl$  position and then calculating the area under the curve of integrated intensity versus  $hkl$  positions, corrected for linear background.

The RIXS measurements of Fig. 4 were performed at the SIX 2-ID Beamline of NSLS-II. Figure 8 shows the XAS at the  $\text{Ni } L_3$  edge which was measured in partial fluorescence yield integrating over an energy window of 800–860 eV and

acquired using the RIXS spectrometer [63]. The high-energy resolution RIXS experiment was performed using the Centurion RIXS spectrometer at the SIX 2-ID Beamline. The combined energy resolution at the  $\text{Ni } L_3$  edge ( $\sim 853$  eV) was  $\Delta E \sim 30$  meV (full width at half maximum). The scattering angle was set to  $2\theta = 150^\circ$  throughout the experiment. The incident angle was  $\theta = 75^\circ$ . The sample was mounted on a wedge to align the transferred moment  $\mathbf{q}$  to the sample  $[111]$  direction.  $\pi$ -polarized light was used to reduce the elastic scattering signal.

### D. Theory

All calculations were performed using spin-polarized density functional theory [64,65] as implemented in the plane-wave-based Vienna *Ab Initio* Simulation Package (VASP 5.4.4) [66]. A plane-wave kinetic energy cutoff of 600 eV was employed for all calculations. An electronic convergence criterion of  $10^{-6}$  eV was used, and all structure models were relaxed until the Hellmann-Feynman forces on each atom were less than  $10^{-2}$  eV/Å. A previous study [67] demonstrated that the rotationally invariant DFT +  $U$  method introduced by Dudarev with an effective

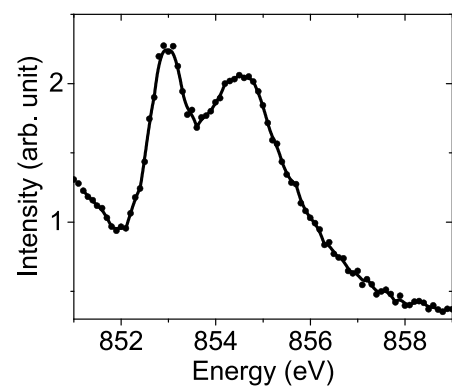


FIG. 8. Sample x-ray absorption of the Ni absorption edge. The chosen 853 eV energy for the RIXS spectra is based on the primary peak in the  $\text{Ni } L_3$  absorption spectra.

Coulomb interaction parameter ( $U_{eff}$ ) = 2 eV and the PBEsol exchange-correlation (XC) functional [68] correctly predicts the insulating and metallic phases of pure RNiO<sub>3</sub>. Furthermore, it was shown different  $U_{eff}$  values have minor effects on crystal geometry [69]. As such, we use this approach for this study. Projected augmented wave (PAW) [70,71] potentials were used with the following valence electronic configurations: Y:  $4s^2 5s^1 4p^6 4d^2$ ; Nd:  $5s^2 6s^2 5p^6 5d^1$ ; La:  $5s^2 6s^2 5p^6 5d^1$ ; Sm:  $5s^2 6s^2 5p^6 5d^1$ ; Gd:  $6s^2 5p^6 5d^1$ ; and O:  $2s^2 2p^4$ . The 4f electrons of rare earth elements were assumed as core electrons; thus we neglected their magnetic ordering by employing PAW potentials corresponding to 3<sup>+</sup> valence states. The ground-state configuration was determined by considering standard spin orientations on the Ni site forming the FM, A-AFM, C-AFM, and G-AFM orderings which correspond to magnetic wave vector  $\mathbf{k} = [0, 0, 0] \frac{\pi}{a}$ ,  $[0, 0, \frac{1}{2}] \frac{\pi}{a}$ ,  $[\frac{1}{2}, \frac{1}{2}, 0] \frac{\pi}{a}$ , and  $[\frac{1}{2}, \frac{1}{2}, \frac{1}{2}] \frac{\pi}{a}$ , respectively. The  $4 \times 4 \times 4$  Monkhorst-Pack set of  $k$  points [72] was used for the Brillouin zone integration for an ANiO<sub>3</sub> formula unit and scaled proportionally for a supercell.

In order to model HVNiO<sub>3</sub> with five different A-site cations and the aforementioned antiferromagnetic spin configurations, a  $2 \times 2 \times 10$  supercell (40 ANiO<sub>3</sub> formula units) was employed [Fig. 3(a)]. The cations were quasirandomly assigned to the A-sites using the special quasirandom structures (SQS) algorithm [73] as implemented in the Alloy Theoretic Automated Toolkit (ATAT) open source software [74]. We consider the displacement of O atoms from their face-centered

positions which is quantified in terms of bond rotation angles ( $180-\theta$ ), where  $\theta$  is the angle among three oxygen ions between two corner-shared oxygen octahedra in the  $ab$  plane [Fig. 3(b) inset].

## ACKNOWLEDGMENTS

Experiment design, sample synthesis, structural and chemical characterization, and computational modeling were supported by the U.S. Department of Energy (DOE), Office of Science, Basic Energy Sciences (BES), Materials Sciences and Engineering Division (MSED). This research used the Soft Inelastic X-ray Scattering (2-ID) and the Coherent Soft X-ray Scattering (23-ID-1) beamlines of the National Synchrotron Light Source II, a U.S. Department of Energy (DOE) Office of Science User Facility, operated for the DOE Office of Science by Brookhaven National Laboratory Contract No. DE-SC0012704. The work at Los Alamos National Laboratory was supported by the NNSA's Laboratory Directed Research and Development Program, and was performed, in part, at the CINT, an Office of Science User Facility operated for the U.S. Department of Energy Office of Science through the Los Alamos National Laboratory. Los Alamos National Laboratory is operated by Triad National Security, LLC, for the National Nuclear Security Administration of U.S. Department of Energy (Contract No. 89233218CNA000001). We also acknowledge resources made available through BNL/LDRD#19-013.

- 
- [1] J. A. Alonso, J. L. García-Muñoz, M. T. Fernández-Díaz, M. A. G. Aranda, M. J. Martínez-Lope, and M. T. Casais, Charge Disproportionation in RNiO<sub>3</sub> Perovskites: Simultaneous Metal-Insulator and Structural Transition in YNiO<sub>3</sub>, *Phys. Rev. Lett.* **82**, 3871 (1999).
- [2] Y. Lu, D. Betto, K. Fürsich, H. Suzuki, H.-H. Kim, G. Cristiani, G. Logvenov, N. B. Brookes, E. Benckiser, M. W. Haverkort *et al.*, Site-Selective Probe of Magnetic Excitations in Rare-Earth Nickelates Using Resonant Inelastic X-Ray Scattering, *Phys. Rev. X* **8**, 031014 (2018).
- [3] S. Catalano *et al.*, Electronic transitions in strained SmNiO<sub>3</sub> thin films, *APL Mater.* **2**, 116110 (2014).
- [4] C. Domínguez, Length scales of interfacial coupling between metal and insulator phases in oxides, *Nat. Mater.* **19**, 1182 (2020).
- [5] M. Kotiuga *et al.*, Carrier localization in perovskite nickelates from oxygen vacancies, *Proc. Natl. Acad. Sci. USA* **116**, 21992 (2019).
- [6] S. Middey, J. Chakhalian, P. Mahadevan, J. W. Freeland, A. J. Millis, and D. D. Sarma, Physics of ultrathin films and heterostructures of rare-earth nickelates, *Annu. Rev. Mater. Res.* **46**, 305 (2016).
- [7] D. Li, K. Lee, B. Y. Wang, M. Osada, S. Crossley, H. R. Lee, Y. Cui, Y. Hikita, and H. Y. Hwang, Superconductivity in an infinite-layer nickelate, *Nature (London)* **572**, 624 (2019).
- [8] M. Osada, B. Y. Wang, B. H. Goodge, S. P. Harvey, K. Lee, D. Li, L. F. Kourkoutis, and H. Y. Hwang, Nickelate superconductivity without rare-earth magnetism: (La, Sr)NiO<sub>2</sub>, *Adv. Mater.* **33**, 2104083 (2021).
- [9] M. Osada, B. Y. Wang, K. Lee, D. Li, and H. Y. Hwang, Phase diagram of infinite layer praseodymium nickelate Pr<sub>1-x</sub>Sr<sub>x</sub>NiO<sub>2</sub> thin films, *Phys. Rev. Mater.* **4**, 121801(R) (2020).
- [10] S. Zeng, C. S. Tang, X. Yin, C. Li, M. Li, Z. Huang, J. Hu, W. Liu, G. J. Omar, H. Jani *et al.*, Phase Diagram and Superconducting Dome of Infinite-Layer Nd<sub>1-x</sub>Sr<sub>x</sub>NiO<sub>2</sub> Thin Films, *Phys. Rev. Lett.* **125**, 147003 (2020).
- [11] J. P. Attfield, A. L. Kharlanov, and J. A. McAllister, Cation effects in doped La<sub>2</sub>CuO<sub>4</sub> superconductors, *Nature (London)* **394**, 157 (1998).
- [12] J. Zhang, A. S. Botana, J. W. Freeland, D. Phelan, H. Zheng, V. Pardo, M. R. Norman, and J. F. Mitchell, Large orbital polarization in a metallic square-planar nickelate, *Nat. Phys.* **13**, 864 (2017).
- [13] G. G. Guzmán-Verri, R. T. Brierley, and P. B. Littlewood, Cooperative elastic fluctuations provide tuning of the metal-insulator transition, *Nature (London)* **576**, 429 (2019).
- [14] R. K. Patel, D. Meyers, X. Liu, P. Mandal, M. Kareev, P. Shafer, J.-W. Kim, P. J. Ryan, S. Middey, and J. Chakhalian, Emergent behavior of LaNiO<sub>3</sub> in short-periodic nickelate superlattices, *APL Mater.* **8**, 041113 (2020).
- [15] J. P. Attfield, 'A' cation control of perovskite properties, *Cryst. Eng.* **5**, 427 (2002).
- [16] R. J. D. Tilley, *Perovskites: Structure-Property Relationships* (Wiley, New York, 2016).
- [17] O. Mustonen, S. Vasala, K. P. Schmidt, E. Sadrollahi, H. C. Walker, I. Terasaki, F. J. Litterst, E. Baggio-Saitovitch, and M. Karppinen, Tuning the  $S = 1/2$  square-lattice antiferromagnet

- $\text{Sr}_2\text{Cu}(\text{Te}_{1-x}\text{W}_x)\text{O}_6$  from Néel order to quantum disorder to columnar order, *Phys. Rev. B* **98**, 064411 (2018).
- [18] F. Otto, Y. Yang, H. Bei, and E. P. George, relative effects of enthalpy and entropy on the phase stability of equiatomic high-entropy alloys, *Acta Mater.* **61**, 2628 (2013).
- [19] C. M. Rost, E. Sacht, T. Borman, A. Moballegh, E. C. Dickey, D. Hou, J. L. Jones, S. Curtarolo, and J.-P. Maria, Entropy-stabilized oxides, *Nat. Commun.* **6**, 8485 (2015).
- [20] B. L. Musicó, D. Gilbert, T. Z. Ward, K. Page, E. George, J. Yan, D. Mandrus, and V. Keppens, The emergent field of high entropy oxides: Design, prospects, challenges, and opportunities for tailoring material properties, *APL Mater.* **8**, 040912 (2020).
- [21] J. Dąbrowa, M. Stygar, A. Mikuła, A. Knapik, K. Mroczka, W. Tejchman, M. Danielewski, and M. Martin, Synthesis and microstructure of the  $(\text{Co}, \text{Cr}, \text{Fe}, \text{Mn}, \text{Ni})_3\text{O}_4$  high entropy oxide characterized by spinel structure, *Mater. Lett.* **216**, 32 (2018).
- [22] B. Musicó, Q. Wright, T. Z. Ward, A. Grutter, E. Arenholz, D. Gilbert, D. Mandrus, and V. Keppens, Tunable magnetic ordering through cation selection in entropic spinel oxides, *Phys. Rev. Mater.* **3**, 104416 (2019).
- [23] Y. Sharma *et al.*, Magnetic texture in insulating single crystal high entropy oxide spinel films, *ACS Appl. Mater. Interfaces* **13**, 17971 (2021).
- [24] R. K. Patel, S. K. Ojha, S. Kumar, A. Saha, P. Mandal, J. W. Freeland, and S. Middey, Epitaxial stabilization of ultra thin films of high entropy perovskite, *Appl. Phys. Lett.* **116**, 071601 (2020).
- [25] Y. Sharma, B. L. Musico, X. Gao, C. Hua, A. F. May, A. Herklotz, A. Rastogi, D. Mandrus, J. Yan, H. N. Lee *et al.*, Single-crystal high entropy perovskite oxide epitaxial films, *Phys. Rev. Mater.* **2**, 060404(R) (2018).
- [26] A. Sarkar, R. Djenadic, D. Wang, C. Hein, R. Kautenburger, O. Clemens, and H. Hahn, Rare earth and transition metal based entropy stabilised perovskite type oxides, *J. Eur. Ceram. Soc.* **38**, 2318 (2018).
- [27] M. Brahlek, A. R. Mazza, K. C. Pitike, E. Skoropata, J. Lapano, G. Eres, V. R. Cooper, and T. Z. Ward, Unexpected crystalline homogeneity from the disordered bond network in  $\text{La}(\text{Cr}_{0.2}\text{Mn}_{0.2}\text{Fe}_{0.2}\text{Co}_{0.2}\text{Ni}_{0.2})\text{O}_3$ , *Phys. Rev. Mater.* **4**, 054407 (2020).
- [28] Y. Sharma *et al.*, High entropy oxide relaxor ferroelectrics, *ACS Appl. Mater. Interfaces* **14**, 11962 (2022).
- [29] C. M. Rost, Z. Rak, D. W. Brenner, and J.-P. Maria, Local structure of the  $\text{Mg}_x\text{Ni}_x\text{Co}_x\text{Cu}_x\text{Zn}_x\text{O}$  ( $x = 0.2$ ) entropy-stabilized oxide: An EXAFS study, *J. Am. Ceram. Soc.* **100**, 2732 (2017).
- [30] Z. Lun *et al.*, Cation-disordered rocksalt-type high-entropy cathodes for Li-ion batteries, *Nat. Mater.* **20**, 214 (2021).
- [31] J. Zhang *et al.*, Long-range antiferromagnetic order in a rocksalt high entropy oxide, *Chem. Mater.* **31**, 3705 (2019).
- [32] B. Jiang, C. A. Bridges, R. R. Unocic, K. C. Pitike, V. R. Cooper, Y. Zhang, D.-Y. Lin, and K. Page, Probing the local site disorder and distortion in pyrochlore high-entropy oxides, *J. Am. Chem. Soc.* **143**, 4193 (2021).
- [33] W. Zhang *et al.*, Applying configurational complexity to the 2D Ruddlesden–Popper crystal structure, *ACS Nano* **14**, 13030 (2020).
- [34] B. L. Musicó, Q. Wright, C. Delzer, T. Z. Ward, C. J. Rawn, D. G. Mandrus, and V. Keppens, Synthesis method comparison of compositionally complex rare earth-based Ruddlesden–Popper  $n = 1T'$ -type cuprates, *J. Am. Ceram. Soc.* **104**, 3750 (2021).
- [35] A. R. Mazza *et al.*, Searching for superconductivity in high entropy oxide Ruddlesden–Popper cuprate films, *J. Vac. Sci. Technol. A* **40**, 013404 (2022).
- [36] D. Bérardan, S. Franger, A. K. Meena, and N. Dragoe, Room temperature lithium superionic conductivity in high entropy oxides, *J. Mater. Chem. A* **4**, 9536 (2016).
- [37] Y. Sharma, Q. Zheng, A. R. Mazza, E. Skoropata, T. Heitmann, Z. Gai, B. Musico, P. F. Miceli, B. C. Sales, V. Keppens *et al.*, Magnetic anisotropy in single-crystal high-entropy perovskite oxide  $\text{La}(\text{Cr}_{0.2}\text{Mn}_{0.2}\text{Fe}_{0.2}\text{Co}_{0.2}\text{Ni}_{0.2})\text{O}_3$  films, *Phys. Rev. Mater.* **4**, 014404 (2020).
- [38] A. R. Mazza *et al.*, Designing magnetism in high entropy oxides, *Adv. Sci.* **9**, 2200391 (2022).
- [39] A. R. Mazza, E. Skoropata, J. Lapano, J. Zhang, Y. Sharma, B. L. Musico, V. Keppens, Z. Gai, M. J. Brahlek, A. Moreo *et al.*, Charge doping effects on magnetic properties of single-crystal  $\text{La}_{1-x}\text{Sr}_x(\text{Cr}_{0.2}\text{Mn}_{0.2}\text{Fe}_{0.2}\text{Co}_{0.2}\text{Ni}_{0.2})\text{O}_3$  ( $0 \leq x \leq 0.5$ ) high-entropy perovskite oxides, *Phys. Rev. B* **104**, 094204 (2021).
- [40] P. V. Vanitha, A. Arulraj, P. N. Santhosh, and C. N. R. Rao, Effect of cation size and disorder on the structure and properties of the rare earth cobaltates,  $\text{Ln}_{0.5}\text{A}_{0.5}\text{CoO}_3$  ( $\text{Ln} = \text{rare earth}$ ,  $\text{A} = \text{Sr}, \text{Ba}$ ), *Chem. Mater.* **12**, 1666 (2000).
- [41] L. M. Rodriguez-Martinez and J. P. Attfield, Cation disorder and size effects in magnetoresistive manganese oxide perovskites, *Phys. Rev. B* **54**, R15622 (1996).
- [42] J. A. McAllister and J. P. Attfield, Cation size control of structure, structural fluctuations, and superconductivity in  $\text{L}_{1-85}\text{M}_{0.15}\text{CuO}_4$ , *Phys. Rev. B* **66**, 014514 (2002).
- [43] B. Chen *et al.*, Spatially controlled octahedral rotations and metal–insulator transitions in nickelate superlattices, *Nano Lett.* **21**, 1295 (2021).
- [44] S. Catalano, M. Gibert, J. Fowlie, J. Íñiguez, J.-M. Triscone, and J. Kreisel, Rare-earth nickelates  $\text{RNiO}_3$ : Thin films and heterostructures, *Rep. Prog. Phys.* **81**, 046501 (2018).
- [45] V. Bisogni *et al.*, Ground-state oxygen holes and the metal–insulator transition in the negative charge-transfer rare-earth nickelates, *Nat. Commun.* **7**, 13017 (2016).
- [46] C. Liu *et al.*, Observation of an antiferromagnetic quantum critical point in high-purity  $\text{LaNiO}_3$ , *Nat. Commun.* **11**, 7 (2020).
- [47] J.-S. Zhou, J. B. Goodenough, and B. Dabrowski, Transition from Curie-Weiss to Enhanced Pauli Paramagnetism in  $\text{RNiO}_3$  ( $R = \text{La}, \text{Pr}, \dots, \text{Gd}$ ), *Phys. Rev. B* **67**, 020404(R) (2003).
- [48] J. Liu *et al.*, Heterointerface engineered electronic and magnetic phases of  $\text{NdNiO}_3$  thin films, *Nat. Commun.* **4**, 2714 (2013).
- [49] S. K. Ojha, S. Ray, T. Das, S. Middey, S. Sarkar, P. Mahadevan, Z. Wang, Y. Zhu, X. Liu, M. Kareev *et al.*, Anomalous electron transport in epitaxial  $\text{NdNiO}_3$  films, *Phys. Rev. B* **99**, 235153 (2019).
- [50] J.-S. Zhou, J. B. Goodenough, and B. Dabrowski, Exchange Interaction in the Insulating Phase of  $\text{RNiO}_3$ , *Phys. Rev. Lett.* **95**, 127204 (2005).
- [51] J. Fowlie, *Electronic and Structural Properties of  $\text{LaNiO}_3$ -Based Heterostructures* (Springer International Publishing, Cham, Switzerland, 2019).



- [52] G. Marshall, A. J. Wooles, D. P. Mills, W. Lewis, A. J. Blake, and S. T. Liddle, Synthesis and characterisation of lanthanide *n*-trimethylsilyl and -mesityl functionalised bis(iminophosphorano)methanides and -methanediides, *Inorganics* **1**, 46 (2013).
- [53] R. D. Shannon, Revised effective ionic radii and systematic studies of interatomic distances in halides and chalcogenides, *Acta Crystallogr., Sect. A* **32**, 751 (1976).
- [54] G. Ghiringhelli, A. Piazzalunga, C. Dallera, T. Schmitt, V. N. Strocov, J. Schlappa, L. Patthey, X. Wang, H. Berger, and M. Grioni, Observation of Two Nondispersive Magnetic Excitations in NiO by Resonant Inelastic Soft-X-Ray Scattering, *Phys. Rev. Lett.* **102**, 027401 (2009).
- [55] M. Medarde, C. Dallera, M. Grioni, B. Delley, F. Vernay, J. Mesot, M. Sikora, J. A. Alonso, and M. J. Martínez-Lope, Charge Disproportionation in *RNiO<sub>3</sub>* Perovskites (*R* = Rare Earth) from High-Resolution X-Ray Absorption Spectroscopy, *Phys. Rev. B* **80**, 245105 (2009).
- [56] N. Dragoe and D. Bérardan, Order emerging from disorder, *Science* **366**, 573 (2019).
- [57] S. J. McCormack and A. Navrotsky, Thermodynamics of high entropy oxides, *Acta Mater.* **202**, 1 (2021).
- [58] G. Anand, A. P. Wynn, C. M. Handley, and C. L. Freeman, Phase stability and distortion in high-entropy oxides, *Acta Mater.* **146**, 119 (2018).
- [59] M. Brahlek *et al.*, What is in a name: Defining “high entropy” oxides, *APL Mater.* **10**, 110902 (2022).
- [60] G. Eres, J. Z. Tischler, C. M. Rouleau, H. N. Lee, H. M. Christen, P. Zschack, and B. C. Larson, Dynamic Scaling and Island Growth Kinetics in Pulsed Laser Deposition of SrTiO<sub>3</sub>, *Phys. Rev. Lett.* **117**, 206102 (2016).
- [61] G. Eres, J. Z. Tischler, C. M. Rouleau, P. Zschack, H. M. Christen, and B. C. Larson, Quantitative determination of energy enhanced interlayer transport in pulsed laser deposition of SrTiO<sub>3</sub>, *Phys. Rev. B* **84**, 195467 (2011).
- [62] J. Z. Tischler, G. Eres, B. C. Larson, C. M. Rouleau, P. Zschack, and D. H. Lowndes, Nonequilibrium Interlayer Transport in Pulsed Laser Deposition, *Phys. Rev. Lett.* **96**, 226104 (2006).
- [63] J. Dvorak, I. Jarrige, V. Bisogni, S. Coburn, and W. Leonhardt, Towards 10 MeV resolution: The design of an ultrahigh resolution soft x-ray RIXS spectrometer, *Rev. Sci. Instrum.* **87**, 115109 (2016).
- [64] A. Zunger, S.-H. Wei, L. G. Ferreira, and J. E. Bernard, Special Quasirandom Structures, *Phys. Rev. Lett.* **65**, 353 (1990).
- [65] A. van de Walle, P. Tiwary, M. de Jong, D. L. Olmsted, M. Asta, A. Dick, D. Shin, Y. Wang, L.-Q. Chen, and Z.-K. Liu, Efficient stochastic generation of special quasirandom structures, *CALPHAD* **42**, 13 (2013).
- [66] P. Hohenberg and W. Kohn, Inhomogeneous electron gas, *Phys. Rev.* **136**, B864 (1964).
- [67] W. Kohn and L. J. Sham, Self-consistent equations including exchange and correlation effects, *Phys. Rev.* **140**, A1133 (1965).
- [68] J. P. Perdew, A. Ruzsinszky, G. I. Csonka, O. A. Vydrov, G. E. Scuseria, L. A. Constantin, X. Zhou, and K. Burke, Restoring the Density-Gradient Expansion for Exchange in Solids and Surfaces, *Phys. Rev. Lett.* **100**, 136406 (2008).
- [69] J. Varignon, M. N. Grisolia, J. Íñiguez, A. Barthélémy, and M. Bibes, complete phase diagram of rare-earth nickelates from first-principles, *npj Quantum Mater.* **2**, 21 (2017).
- [70] P. Yoo and P. Liao, First principles study on hydrogen doping induced metal-to-insulator transition in rare earth nickelates *RNiO<sub>3</sub>* (*R* = Pr, Nd, Sm, Eu, Gd, Tb, Dy, Yb), *Phys. Chem. Chem. Phys.* **22**, 6888 (2020).
- [71] P. E. Blöchl, Projector augmented-wave method, *Phys. Rev. B* **50**, 17953 (1994).
- [72] G. Kresse and D. Joubert, From ultrasoft pseudopotentials to the projector augmented-wave method, *Phys. Rev. B* **59**, 1758 (1999).
- [73] K. Yamauchi, F. Freimuth, S. Blügel, and S. Picozzi, Magnetically induced ferroelectricity in orthorhombic manganites: Microscopic origin and chemical trends, *Phys. Rev. B* **78**, 014403 (2008).
- [74] A. van de Walle, M. Asta, and G. Ceder, The alloy theoretic automated toolkit: A user guide, *CALPHAD* **26**, 539 (2002).